Optics Letters

Photoacoustic imaging methodology for the optical characterization of contact lenses

George J. Tserevelakis,[1] Margarita Tsagkaraki,[2] Miltiadis K. Tsilimbaris,[2] Sotiris Plainis,[2] and Giannis Zacharakis[1,*]

[1]Institute of Electronic Structure and Laser, Foundation for Research and Technology Hellas, Heraklion, Crete, Greece
[2]Laboratory of Vision and Optics, School of Medicine, University of Crete, Heraklion, Crete, Greece
*Corresponding author: zahari@iesl.forth.gr

Received 14 August 2017; accepted 12 September 2017; posted 18 September 2017 (Doc. ID 303700); published 5 October 2017

We demonstrate photoacoustic microscopy as a metrology method for the optical characterization and quality control of contact lenses (CLs). Dual-wavelength excitation is applied to CLs tinted on both sides with two thin ink layers, each of them possessing distinctly different optical absorption properties. Thus, the method is capable of measuring the elevation maps of both CL surfaces during two subsequent imaging sessions and extracting the CL thickness, curvatures, and dioptric power. We show that such an easily implementable technique provides robust, high-precision, cost-effective three-dimensional imaging and characterization of both rigid and soft CLs, which renders it highly favorable for a broad range of applications.

OCIS codes: (110.0180) Microscopy; (110.5120) Photoacoustic imaging; (330.7325) Visual optics, metrology.

https://doi.org/10.1364/OL.42.004111

Contact lenses (CLs) represent a significant and increasing share in vision correction, especially following the introduction of new materials, optical designs, and manufacturing processes. Therefore, the demand for cost-effective accurate metrology and quality control methods is very high [1,2]. Various approaches have been used for measuring the power profiles of lenses, including small-aperture focimetry [3] and instruments based on Moiré, interferometric [4], Schlieren [5], Hartmann–Shack [6,7], and optical coherence tomography methodologies [8–10]. With most of these techniques, soft CLs are placed in a saline-filled wet cell, and the derived powers are corrected to air values using a factor that allows for the different immersion index. Apart from the problem of avoiding lens distortion in the cell, major limitations often include modest lateral resolution and, with the Hartmann–Shack method, difficulties in relating the image spots to the appropriate lenslets, particularly when the lens power profile displays abrupt discontinuities [11]. More recently, profiles of soft CLs have been measured using ptychography, a diffraction-based method [12] (PhaseFocus Lens Profiler; Phase Focus, Sheffield, UK). Ptychographic imaging is achieved by recording a series of diffraction patterns from neighboring points on the lens and is used to reconstruct the lens thickness profile and, hence, its power profiles with a high resolution [13].

Herein, we present the development of a novel methodology, based on photoacoustic (PA) imaging, as a metrology tool for the optical characterization and qualitative inspection of CLs. PA modality provides imaging contrast by taking advantage of the well-known PA effect, during which acoustic waves are generated following the absorption of intensity-modulated optical radiation by a material. At microscopic scales, PA imaging has been widely used to provide detailed *in vivo* information regarding biological structures such as small tumours, capillaries, and melanoma cells, under intense scattering conditions [14]. Thus, by exploiting this powerful biomedical imaging technique for CL measurements, we demonstrate that its application potential can be successfully extended into the optometry research field.

The employed custom-built PA microscopy setup (Fig. 1) integrates a diode-pumped Nd:YAG laser emitting at 1064 nm (QIR-1064-200-S, CrystaLaser LC, Reno, Nevada, U.S.; pulse energy, 29.4 μJ; pulse duration, 10 ns; selected repetition rate, 6.78 kHz) to excite the PA signals. The beam is focused on a Lithium triborate second-harmonic generation (SHG) crystal (Castech, Inc., Fuzhou, China) to be partially transformed into a 532 nm visible wavelength and is subsequently collimated and expanded by a second lens in a ∼6× telescope configuration. A filter wheel incorporating two bandpass filters (FL1064-10, Thorlabs, Newton, New Jersey, U.S. and FF01-531/40-25, Semrock, Rochester, New York, U.S.) is used to interchange between infrared and visible excitation of the CL. The selected irradiation beam is adequately attenuated through a set of neutral density filters in order to avoid any photodamage effects, before being guided towards a modified inverted microscope (Labovert, Leitz, Wetzlar, Germany) serving as a platform for the developed imaging system. A low numerical aperture (NA) objective lens (Achromat 8×, LOMO, St. Petersburg, Russia; air immersion, NA: 0.2) focuses the beam loosely through a round, optically transparent window (∼2 cm) of a sample holder filled with distilled water, which provides the necessary acoustic coupling for the efficient PA wave

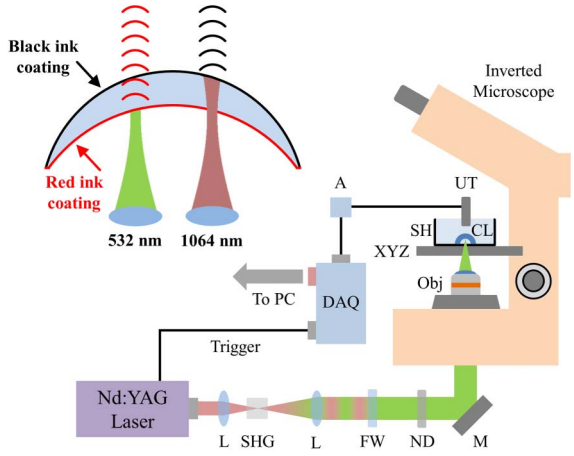

Fig. 1. Dual-wavelength excitation PA microscopy setup for the characterization of a double-coated CL. L, lens; SHG, second-harmonic generation crystal; FW, filter wheel; ND, neutral density filters; M, mirror; Obj, objective lens; XYZ, 3D translational stage; SH, sample holder; CL, contact lens; UT, ultrasonic transducer; A, amplifier; DAQ, data acquisition card.

propagation and detection. The CL to be measured is placed at the center of the window and brought into focus using the manual Z-stage control of the microscope. A 20 MHz central frequency spherically focused ultrasonic transducer (V373-SU, Olympus, Tokyo, Japan; effective bandwidth, 13–33 MHz; focal distance, 32 mm) is immersed into the coupling medium to detect the generated PA waves in a confocal and coaxial configuration with respect to the illumination.

The generated voltage signal is enhanced by a low noise radio-frequency (RF) amplifier (AU-1291, Miteq, New York, U.S.; gain 63 dB) and, subsequently, recorded by a data acquisition (DAQ card (PCIe-9852, ADLINK, Taipei, Taiwan; sampling rate, 200 MS/s; bandwidth, 90 MHz) synchronized with the laser trigger. The point-by-point imaging of the CL is achieved using a high-precision motorized XY stage (8MTF-75LS05, Standa, Vilnius, Lithuania), which raster scans the sample holder over the optical focus. A typical CL scanning session covers an approximate volume of 13 mm × 13 mm × 3 mm sampled with a voxel size equal to 65 μm × 65 μm × 15 μm in around 10 min per reconstructed surface.

Prior to the PA measurements, both of the CL surfaces are coated using a soft-tipped round paintbrush, with two types of thin ink layers, each of them demonstrating significantly different optical absorption properties in the near-infrared range. More specifically, the anterior surface is coated with black ink (extracted from a Mitsubishi Pencil UNI Marker, No. 520 F) of relatively high absorption in the visible and near-infrared wavelengths, whereas the respective posterior surface is tinted with a red colored ink (extracted from a Lumocolor permanent marker 350) being virtually transparent in the near-infrared part of the spectrum. The absorption spectra for the two types of ink (Fig. 2) reveal comparable absorbance magnitudes at 532 nm, but a seven-fold higher value for the black coating compared to the red one at 1064 nm. In this manner, the dual-wavelength excitation PA microscopy system is capable of mapping both of the CL surfaces during two subsequent distinct imaging sessions with the use of a single excitation source.

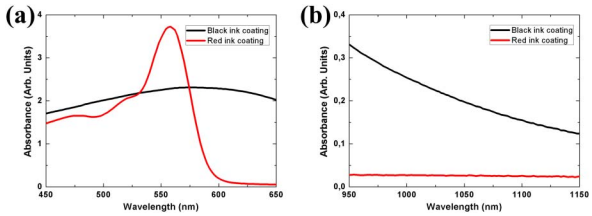

Fig. 2. Absorption spectra of black and red ink coatings for (a) 450–650 nm and (b) 950–1150 nm wavelength ranges.

As a first step, the system was calibrated using an optically transparent hemispherical phantom of known geometrical properties. The phantom was generated by immersing an industrially made spherical metallic marble (radius: 7.80 ± 0.01 mm) into liquid silicone medium, which was left to solidify for several hours. Following the removal of the marble, the resulting mold was then filled with resin in order to provide the CL-mimicking specimen. The phantom's surface was coated with the black ink and, subsequently, measured by employing the 1064 nm wavelength. The calibration process is essential for improving the reconstruction accuracy due to the relative uncertainty regarding the exact ultrasonic speed in distilled water (~1480 m/s), as well as the possible translational motion errors during the mechanical raster scanning. Following the end of the calibration, we proceeded to the surface measurements of a double-coated rigid gas permeable (RGP) CL (power: −3.00 D, base curve [BC], 7.75 mm, Menicon Z Comfort, Menicon Co., Ltd., Nagoya, Japan). The refractive power and the BC value of the CL were measured prior to the PA imaging session by an auto-lensmeter (LM1000, Nidek Co., Ltd., Japan) and an autorefracto-keratometer (MRK 3100P, Huvitz Co., Ltd., Korea), respectively, validating the nominal parameters provided by the manufacturer. As a common practice in PA microscopy, each of the recorded waveforms was Hilbert-transformed, and the modulus of the complex result was used for the representation of the axial profile for each lateral scan position. In this manner, the temporal position of the axial profile's maximum value could delineate the surface of interest point by point.

Nevertheless, such high-precision measurements through the intrinsically hybrid PA effect require a correction for optical and acoustic distortions originating from the different refractive and mechanical properties of the CL material, compared to the surrounding immersion medium. As to the anterior surface measurement [Fig. 3(a)], the incoming excitation ray is bent according to Snell's law due to the refractive index difference between the CL ($n2$) and the distilled water ($n1$). If $\theta 1$ and $\theta 2$ are the angles of incidence and refraction, respectively, and $\theta 3$ is equal to $\theta 1 - \theta 2$, it can be easily derived under a small angle approximation in which

$$\Delta x = \frac{d\frac{x}{R}\left(1 - \frac{n1}{n2}\right)}{1 + \frac{n1}{n2}\left(\frac{x}{R}\right)^2}, \tag{1}$$

where Δx is the lateral deviation of the incident ray on the anterior surface level, x is the distance measured from the lens symmetry axis, R is the radius of curvature for the posterior surface, and d is a vertical distance equal to $\Delta x/\tan(\theta 3)$. As a direct consequence, for the typical case where $n2 > n1$, the induced refractive error results in a steeper anterior surface estimation due to the lateral distortion. To compensate for this

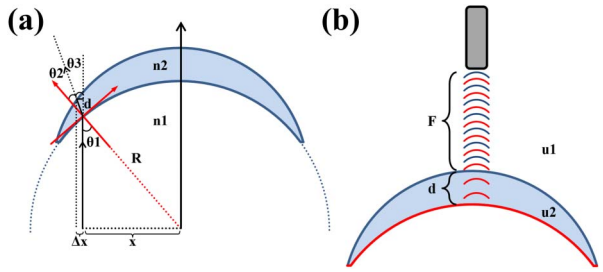

Fig. 3. Optical and acoustic distortion errors affecting CL surface reconstruction. (a) Refractive index mismatch between the lens material ($n2$) and the surrounding medium ($n1$) bends the incoming rays to introduce a lateral error Δx during the anterior surface measurement. (b) Transmission of PA waves through the lens material at speed $u2$ generates an axial distortion when measuring the posterior surface of the lens (red color).

deviation, we have multiplied the lateral dimensions of each voxel by a correction factor $M_A = 1 + (\Delta x/x)$ prior to the final optical zone reconstruction which, for typical parameter values ($x = 3.25$ mm, $R = 7.5$ mm, $d = 0.15$ mm, and $n1 = 1.33$, $n2 = 1.44$), is calculated to be ~1.0013.

Regarding the posterior surface measurement [Fig. 3(b)], an axial distortion is generated during the propagation of the respective PA waves through the CL volume at a different speed ($u2$) compared to the immersion medium ($u1$). If we assume that the path length through the CL is equal to d and F is the relative distance between the ultrasonic detector and the anterior surface of the lens, a path-weighted average ultrasonic speed $\bar{u}$ will be given by the expression $\bar{u} = [d/(F + d)] * u2 + [F/(F + d)] * u1$. For approximate values of the involved parameters ($d = 0.15$ mm, $F = 30$ mm, $u1 = 1480$ m/s, and $u2 = 2500$ m/s), $\bar{u}$ is estimated to be around 1485 m/s. Consequently, a posterior surface correction factor $M_P = \bar{u}/u1$ is introduced as a multiplying constant in the axial voxel size, with a typical value ~1.0034. In this context, the posterior CL surface is adjusted for the acoustic propagation distortion which, if not compensated for, tends to flatten the respective reconstruction. It has to be mentioned that the approximations introduced into the estimation of the correction factors have a negligible to slight impact on the determination of the geometrical and optical parameters for a broad range of typical CLs.

Having taken into account the corrections described above, the collected data were processed via a custom-developed MATLAB code in order to extract the required geometrical information for the characterization of the CL under investigation. The measured elevation map for the optical zone region (~6.5 mm diameter) of the anterior surface is presented in Fig. 4(a), whereas Fig. 4(b) shows the respective second-order polynomial fitting reconstruction ($R^2 = 0.998$) having the typical form $S(x, y) = Ax^2 + By^2 + Cxy + Dx + Ey + F$. The radius of curvature map $R(x, y)$ depicted in Fig. 4(c) was subsequently calculated as the reciprocal of the mean curvature H for the fitted surface S which, in Cartesian coordinates, can be analytically expressed as

$$H = \frac{\left(1 + \left(\frac{\partial S}{\partial x}\right)^2\right)\frac{\partial^2 S}{\partial y^2} - 2\frac{\partial S}{\partial x}\frac{\partial S}{\partial y}\frac{\partial^2 S}{\partial x \partial y} + \left(1 + \left(\frac{\partial S}{\partial y}\right)^2\right)\frac{\partial^2 S}{\partial x^2}}{2\left(1 + \left(\frac{\partial S}{\partial x}\right)^2 + \left(\frac{\partial S}{\partial y}\right)^2\right)^{3/2}}. \quad (2)$$

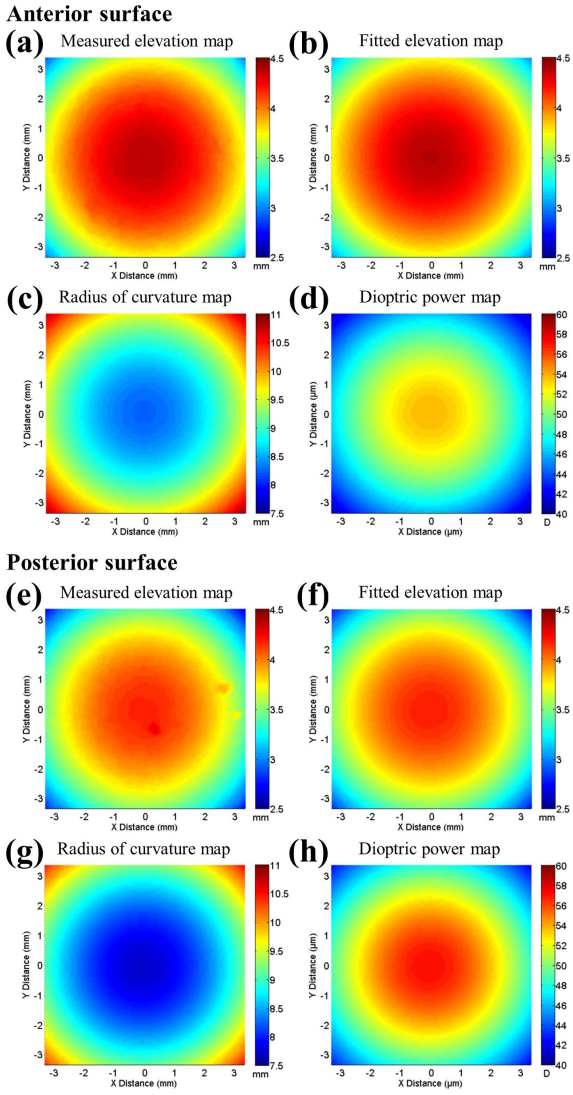

Fig. 4. Characterization of a double-coated RGP CL. (a)–(d) Anterior surface maps for the measured and the polynomially fitted elevation, the calculated radius of curvature, and the corresponding dioptric power. (e)–(h) Respective maps for the posterior surface of the lens.

In this manner, the radius of curvature $R1$ at the center of the CL was found to be 8.25 ± 0.01 mm. The precision tolerance ΔR (95% confidence level assumed) was calculated using the formula $\Delta R = \pm 1.96 * S/N^{1/2}$, where S is the standard deviation of N sequential measurements ($N = 5$, $S = 0.014$ mm). The dioptric power map $P(x, y)$ of the anterior CL surface [Fig. 4(d)] was then directly determined through the common expression $P(x, y) = 10^3(n - 1)/R(x, y)$, where $n = 1.443$, as provided by the lens manufacturer.

Thus, a dioptric power $P1 = 53.70 \pm 0.08$ D was calculated at the center of the lens, whereas the respective precision tolerance was estimated by the equation $\Delta P = \pm 10^3(n - 1)\Delta R/R^2$. In an analogous procedure, similar maps were generated for the posterior CL surface, as explicitly shown in Figs. 4(e)–4(h). Following the polynomial fitting ($R^2 = 0.999$), the radius of curvature $R2$ at the lens center was determined to be 7.75 ± 0.01 mm ($N = 5$, $S = 0.014$ mm), which is identical to the

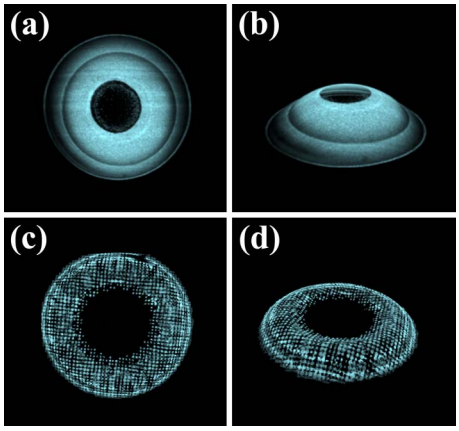

Fig. 5. 3D renderings of industrially tinted soft CLs. (a) and (b) Aspects of a +22.50 D homogeneously colored CL. (c) and (d) Similar aspects of a cosmetic CL without refractive correction.

BC value provided by the manufacturer. Furthermore, the dioptric power $P2$ was estimated at -57.16 ± 0.09 D, whereas the CL central thickness d resulted from the subtraction of the maximum elevation values for the two fitted surfaces ($d = 0.18 \pm 0.01$ mm, manufacturer's given value: 0.17 mm). The total refractive power P of the lens P, was calculated using Gullstrand's formula $P = P1 + P2 - 10^{-3}P1 * P2 * (d/n)$ at -3.08 ± 0.12 D, assuming that the measurement uncertainty arises predominantly from the combined uncertainties in $P1$ and $P2$. The estimated refractive power was very close to its nominal value (−3.00 D), thus confirming the high reliability of the proposed CL characterization technique. Furthermore, it has to be highlighted that the achieved precision tolerance of the followed metrology approach meets the ISO requirements regarding the measurement standards of RGP lenses [15].

Nevertheless, the PA imaging methodology can be also applied to soft CLs, provided that the tinting procedure is performed in a more sophisticated manner which ensures that it will not affect the original geometrical and refractive properties of the lens. To demonstrate the potential applicability of our approach in such a case, we proceeded to the three-dimensional (3D) reconstruction of two industrially tinted soft CLs, following their excitation using the 532 nm wavelength. Figures 5(a) and 5(b) show different aspects of a homogeneously colored soft CL (Troy T74 brown 75%, +22.50 D, Menicon Ltd., Northampton, England), specially designed for aphakic patients with aniridia. The recorded PA signals arise predominantly from the posterior CL surface, since the incident laser radiation is strongly absorbed by the homogeneously distributed pigment, thus limiting the optical penetration within the volume of the lens.

On the other hand, Figs. 5(c) and 5(d) depict views of a cosmetically tinted soft CL (AIR OPTIX colors, brown, plano power, Alcon Laboratories Inc., Fort Worth, Texas, U.S.), revealing clearly the dotted coloration pattern which simulates the pigmentation of the eye's iris. It is observed that in both of the investigated CLs, the optical zone does not generate any PA signals due to the complete absence of tint in this region.

In conclusion, we have presented a novel universal methodology based on the PA effect for the precise optical characterization and 3D imaging of both RGP and soft CLs. The implementation simplicity, as well as the robustness of the proposed technique compared to interferometric measurements, renders it suitable for a broad range of industrial and clinical applications regarding CL quality inspection and optimization. The precision and speed of the PA measurements could be further improved in an upgraded version of the present setup, integrating state-of-the-art components such as broadband ultrasonic detectors and galvanometer optical scanners. Furthermore, the total cost of the setup can be drastically reduced by adopting a frequency domain PA microscopy approach, incorporating low-budget CW laser sources at multiple excitation lines. Finally, data analysis can also be extended in the direction of higher-order optical aberrations measurement, the study of soft CL fitting/flexure on the eye, and the investigation of more complex profiles such as the multifocal CLs used in presbyopia correction.

Funding. Seventh Framework Programme (FP7) Marie Curie ITN "OILTEBIA" project (PITN-GA-2012-317526); H2020 Laserlab Europe (EC-GA 654148).

Acknowledgment. The authors would like to thank Ms. Antigoni Papadaki for recording the absorption spectra shown in Fig. 2 and Ms. Stella Avtzi for generating the calibration phantom. All lenses were supplied free by the manufacturers (Menicon, Alcon).

REFERENCES

1. J. T. Barr and G. E. Lowther, Am. J. Optom. Physiol. Opt. **54**, 809 (1977).
2. S. Plainis and W. N. Charman, Optom. Vis. Sci. **75**, 44 (1998).
3. C. E. Campbell, Optom. Vis. Sci. **86**, 900 (2009).
4. A. Plakitsi and W. N. Charman, Contact Lens Anterior Eye **20**, 97 (1997).
5. L. Joannes, T. Hough, X. Hutsebaut, X. Dubois, R. Ligot, B. Saoul, P. Van Donink, and K. De Coninck, Contact Lens Anterior Eye **33**, 3 (2010).
6. P. Kollbaum, M. Jansen, L. Thibos, and A. Bradley, Optom. Vis. Sci. **85**, E817 (2008).
7. R. C. Bakaraju, K. Ehrmann, A. Ho, and E. Papas, Optom. Vis. Sci. **87**, 1009 (2010).
8. B. R. Davidson and J. K. Barton, J. Biomed. Opt. **15**, 016009 (2010).
9. M. Shen, M. R. Wang, J. Wang, Y. Yuan, and F. Chen, Eye Contact Lens **36**, 73 (2010).
10. K. Karnowski, I. Grulkowski, N. Mohan, I. Cox, and M. Wojtkowski, Opt. Lett. **39**, 4727 (2014).
11. C. E. Campbell, J. Refractive Surg. **24**, 308 (2008).
12. S. Plainis, D. A. Atchinson, and W. N. Charman, Optom. Vis. Sci. **90**, 1066 (2013).
13. A. M. Maiden, M. J. Humphry, F. Zhang, and J. M. Rodenburg, J. Opt. Soc. Am. A **28**, 604 (2011).
14. J. Yao and L. V. Wang, Laser Photon. Rev. **7**, 758 (2013).
15. R. M. Pearson, Clin. Exp. Optom. **91**, 379 (2008).